Eur. Phys. J. D **35**, 567–577 (2005)
DOI: 10.1140/epjd/e2005-00220-8

THE EUROPEAN PHYSICAL JOURNAL D

Electron impact ionization of atomic clusters in ultraintense laser fields

A. Heidenreich, I. Last, and J. Jortner[a]

School of Chemistry, Tel Aviv University, Ramat Aviv, 69978 Tel Aviv, Israel

Received 9 May 2005
Published online 9 August 2005 –

Abstract. In this paper we report on inner ionization of Xe_n clusters ($n = 55-2171$) in ultraintense Gaussian laser fields (peak intensity $I = 10^{15}-10^{20}$ Wcm^{-2}, pulse width $\tau = 25$ fs, frequency 0.35 fs^{-1}). The cluster inner ionization process is induced by the barrier suppression ionization (BSI) mechanism and by electron impact ionization (EII), which occurs sequentially with the BSI. We address electron impact ionization of clusters, which pertains to inelastic reactive processes of the high-energy (100 eV–1 keV per electron) nanoplasma. We utilized experimental data for the energy dependence of the electron impact ionization cross-sections of Xe^{j+} ($j = 1-10$) ions, which were fit by an empirical three-parameter Lotz-type equation, to explore EII in clusters by molecular dynamics simulations. Information was obtained on the yields and time-resolved dynamics of the EII levels (i.e., number n_{imp} of electrons per cluster atom) in the Xe_n clusters and their dependence on the laser intensity and cluster size. The relative long-time ($t = 90$ fs) yields for EII, n_{imp}/n_{ii} (where n_{ii} is the total inner ionization yield) are rather low and increase with decreasing the laser intensity. In the intensity range $I = 10^{15}-10^{16}$ Wcm^{-2}, $n_{imp}/n_{ii} = 0.21$ for $n = 2171$ and $n_{imp}/n_{ii} = 0.09-0.14$ for $n = 459$, while for $I = 10^{18}-10^{20}$ Wcm^{-2}, $n_{imp}/n_{ii} = 0.01-0.05$. The difference Δn_{imp} between the EII yield at long time and at the termination of the laser pulse reflects on ionization dynamics by the nanoplasma when the laser pulse is switched off. For Xe_{2171} in the lower intensity domain, $\Delta n_{imp} = 0.9$ at $I = 10^{15}$ Wcm^{-2} and $\Delta n_{imp} = 0.4$ at 10^{16} Wcm^{-2}, reflecting on EII by the persistent nanoplasma under "laser free" conditions, while in the higher intensity domain of $I = 10^{17}-10^{18}$ Wcm^{-2}, Δn_{imp} is negligibly small due to the depletion of the transient nanoplasma.

PACS. 34.80.Gs Molecular excitation and ionization by electron impact – 36.40.Qv Stability and fragmentation of clusters – 36.40.Wa Charged clusters

Highlight Paper

1 Introduction

Extremely multicharged elemental and molecular clusters, e.g., Xe_n, $(H_2)_n$, $(D_2)_n$, $(H_2O)_n$, $(D_2O)_n$, $(CH_4)_n$, $(CD_4)_n$ and $(DI)_n$, can be prepared by the interactions of these clusters with ultrashort (pulse temporal length $\tau = 10-100$ fs) and ultraintense (peak intensity $I = 10^{15}-10^{20}$ Wcm^{-2}) laser pulses. Extremely high multielectron ionization processes involve the removal of valence electrons or the complete stripping of all the electrons in light first-row atoms or molecules [1–4] with the formation of ionic clusters, e.g., $(D^+)_n$, $(H^+)_n$, $(D_2^+O^{q+})_n$, $(H_2^+O^{q+})_n$ ($q = 6-8$), $(C^{q+}D_4^+)_n$, $(C^{q+}H_4^+)_n$ ($q = 4-6$), or the formation of highly charged ionic clusters, e.g., $(Xe^{q+})_n$ ($q = 5-36$) [5–15] or $(D^+I^{q+})_n$ and $(H^+I^{q+})_n$ ($q = 4-35$) [16,17], which are produced from heavy atoms. These ionic clusters are unstable towards Coulomb explosion [18–25]. Clusters constitute large, finite systems with a density comparable to that of the solid or liquid condensed phase. While the coupling of macroscopic dense matter, e.g., solids or liquids, with ultraintense laser fields is blurred by the effects of the formation of an inhomogeneous dense plasma, isochoric heating, beam self-focusing and radiative continuum production [26,27], the response of clusters (whose size is considerably smaller than the laser wavelength) to ultraintense laser fields triggers well-characterized ultrafast dynamics of electrons (on the time scale of $\lesssim$1–50 fs) and highly charged ions or nuclei (on the time scale of $\sim$10–100 fs). The compound multielectron ionization mechanism of clusters involves three sequential-parallel processes of inner ionization, nanoplasma formation and outer ionization. Inner ionization results in the formation of a charged, energetic nanoplasma (electron energies of $\sim$100 eV–10 keV) within the cluster or its vicinity, which is followed by the partial or complete outer ionization of the nanoplasma. These phenomena constitute a new realm of electron dynamics driven by an ultraintense laser field on the femtosecond

[a] e-mail: jortner@chemsg1.tau.ac.il

time scale [28]. The cluster inner ionization process is induced by two mechanisms.

(A) The barrier suppression ionization (BSI) mechanism. The BSI in clusters is driven by a composite, effective field consisting of the superposition of the laser field and of the inner fields, which are generated by electrostatic interactions with the ions and with the nanoplasma electrons. The inner field contributions involve the ignition effects [29], which increase the effective field by the contribution of the ions, and the screening effects, which decrease the effective field of the ions by the nanoplasma electrons.

(B) Electron impact ionization (EII) mechanism. In parallel with the BSI mechanism, the EII processes prevail. Inner cluster ionization by electron impact manifests additional dynamic effects of the nanoplasma electrons, which are involved in inelastic collisions. Cross-sections for impact ionization of isolated atoms were described using Lotz's model [30]. Last and Jortner used this model for EII of atoms and ions in clusters. This approach, which was previously utilized [19] for estimates of the contribution of impact ionization of the cluster inner ionization yields, rested on 'intelligent guesses' for the parameters which appear in the Lotz model. Accordingly, only qualitative conclusions regarding the yield of EII processes could be inferred.

To provide estimates of EII yields in clusters, reliable input information for the EII cross-sections of the constituents are required. In this paper we address EII dynamics and yields in clusters. We utilize experimental data for the energy dependence of electron impact ionization cross-sections of Xe^{j+} ($j = 1-10$) ions to explore electron impact ionization yields in Xe_n ($n = 55-2171$) clusters. We report on the yields and on the time-resolved dynamics of EII in Xe_n clusters and their dependence on the laser intensity and cluster size. From the practical point of view, in the context of total yields for inner ionization, it is important to assess the yield for EII (mechanism (B)) relative to the yield for the BSI process (mechanism (A)). From the point of view of methodology, electron impact ionization of clusters provides new features of inelastic reactive processes of the nanoplasma coupled to an ultraintense laser field.

2 Methodology of simulations of inner ionization and nanoplasma response of coupled cluster-laser systems

We followed the simulation procedure for high-energy electron dynamics and for nuclear (ion) dynamics previously developed by Last and Jortner [19]. Briefly, the laser electric field F_ℓ was taken as

$$F_\ell = F_{\ell 0}(t)\cos(2\pi\nu t + \varphi_0) \quad (1)$$

Table 1. Intensity dependences of the laser pulse truncation time t_s for Xe_n clusters coupled to a Gaussian laser pulse ($\nu = 0.35$ fs^{-1}, $\tau = 25$ fs).

I(Wcm^{-2})	t_s(fs)
10^{15}	–12.5
10^{16}	–23.1
10^{17}	–28.3
10^{18}	–32.4
10^{19}	–36.4
10^{20}	–39.6

being characterized by a Gaussian shaped envelope function of the pulse

$$F_{\ell 0}(t) = F_M \exp[-2.773(t/\tau)^2] \quad (2)$$

with the parameters of frequency $\nu = 0.35$ fs^{-1} (photon energy of 1.44 eV), phase $\varphi_0 = 0$ and temporal width $\tau = 25$ fs (FWHM of the intensity profile of 18 fs). The electric field maximum F_M is related to the peak intensity I (in Wcm^{-2}) by

$$|eF_M| = 2.745 \times 10^{-7}(I^{1/2}) \text{ eV Å}^{-1}. \quad (3)$$

The laser field, equations (1) and (2), is defined in the temporal range $t > -\infty$, and the peak of the laser pulse is attained at $t = 0$. An initially truncated Gaussian pulse was used in the simulations, with the initial laser field $F_\ell = F_s$ being located at the finite (negative) time $t = t_s$. For Xe_n atomic clusters $F_s = F^{th}$, where F^{th} is the threshold field for the first (single electron) ionization of each Xe atom. At the initial laser field F_s [31] where $t = t_s$, all the cluster atoms are taken as singly charged ions, with the electrons initially located at $r = x_b$ from each ionic center, where x_b is the characteristic BSI barrier distance. Typical values of t_s for Xe_n clusters are given in Table 1. Mechanism (A) for the cluster inner ionization, which is driven by a composite field consisting of the laser field and the inner field, was described in terms of the BSI for each constituent. When the conditions for BSI of an ion in the composite field are satisfied, the inner ionization event is initiated by locating the removed electron at x_b. Multielectron ionization is then realized in a sequential way, with one electron being removed at each inner ionization time step of 20 attoseconds [19,31]. The choice of this (arbitrary) ultrashort time step rests on the assumption that in the ultrahigh intensity domain used herein ($I \geq 10^{15}$ Wcm^{-2}) electron tunneling effects on the BSI are negligible. The additional contribution to the inner ionization, which originates from EII (mechanism (B)), will be described in Section 3. The simulations of the molecular dynamics of the energetic electrons and of the ions were performed by classical molecular dynamics, incorporating electron-electron, electron-ion, ion-ion and electron/ion-laser interactions [31]. High-energy electron dynamics included relativistic effects and were subjected to magnetic effects for electron-laser interactions [31]. These simulation results provide a complete picture of electron-nuclear dynamics, including hydrodynamic effects.

Highlight Paper

3 Electron impact ionization of Xe_n clusters

3.1 Cross-sections for electron impact ionization of Xe_n clusters

In our simulations we have included electron impact single ionization processes

$$Xe^{j+} + e \rightarrow Xe^{(j+1)+} + 2e \tag{4}$$

for the formation of the nanoplasma, while electron impact multi ionization processes [32]

$$Xe^{j+} + e \rightarrow Xe^{(j+m)+} + (m+1)e; \quad m > 1 \tag{5}$$

have been disregarded. The incorporation of electron impact requires the knowledge of the corresponding electron impact cross-sections. Experimental data for electron impact cross-sections $\sigma_n(E)$ as functions of the impact energy E are available up to $j = 10$ [33–37] (i.e., up to 700 eV for $j = 1{-}4$, up to 1400 eV for $j = 5$ and 7, up to $E = 2000$ eV for $j = 8$, and up to $E = 5000$ eV for $j = 9$ and 10). To have a closed expression which allows to interpolate the cross-sections and to extrapolate them to higher energies, we employed the empirical Lotz formula [38] for the electron impact cross-sections

$$\sigma_j(E) = \sum\nolimits_i a_i q_i \frac{\ln(E/P_i)}{EP_i} \{1 - b_i \exp[-c_i(E/P_i - 1)]\}, \tag{6}$$

where E is the impact energy of the impinging electron, P_i is the ionization energy of the ith electron shell, q_i is the number of electrons in shell i, and a_i, b_i, c_i are empirical parameters. We fitted the experimental data to a simplified version of the Lotz formula, in which only the first term $i = 1$ of equation (6) is considered

$$\sigma_j(E) = aq \frac{\ln(E/P)}{EP} \{1 - b \exp[-c(E/P - 1)]\}. \tag{7}$$

Equation (7) requires the knowledge of the ionization energy, which was taken from reference [39], and three parameters aq, b and c for each ionization level, treating aq as a single parameter. The parameters aq were determined from experimental data points at high impact energies $E \gg P$, where equation (4) simplifies to

$$\sigma_j(E) = aq \frac{\ln(E/P)}{EP}. \tag{8}$$

Subsequently, the values of b and c were adjusted so that the empirical function, equation (7), also fits data points at low energies. Figure 1 presents the fitted model functions together with the experimental data points and the parameter values. For comparison, the curves of the high energy limit function, equation (8), are included, showing the effect of the exponential term of equation (7). Since for the ionization of Xe^{7+} no experimental electron impact cross-sections are available, we chose the aq parameter such that for high energies the cross-sections assume an average of the Xe^{6+} and Xe^{8+} values (Fig. 1b). Since the lack of experimental data makes a further refinement meaningless, b and c were set to zero in this case.

From the fitting parameters for each single electron ionization process, which are assembled in Figure 1, the following conclusions emerge. (i) The parameter aq varies in a rather abrupt way from $aq = 2.4{-}2.9 \times 10^{-13}$ cm^2(eV)^2 for $j = 1{-}4$ to $6.8{-}9.4 \times 10^{-13}$ cm^2(eV)^2 for $j = 5{-}10$, where in each domain the variations of aq are irregular with increasing j. Thus the variations of aq cannot be identified with a product of a constant parameter a and some effective number q of electrons, which is expected to change regularly with increasing j. (ii) With the exception of Xe^{5+} (Fig. 1b), the experimental cross-sections are higher than predicted by the high-energy limit function, equation (8). For this reason our values of the b parameter are negative except for Xe^{5+}, unlike in the work of Lotz [30,38]. (iii) The choice of the parameters b and c is not unique, as a variation of b can be compensated to some extent by an appropriate modification of c. Since in this work b and c were treated as fitting parameters, the parameter set b, c depends largely on the choice whether a better agreement with the initial sharp increase or the subsequent drop-off of the experimental cross-section is preferred. Under these conditions it is not surprising that the parameters b and c do not exhibit a trend for increasing j. (iv) In view of the irregular behavior of aq, b and c for Xe^+ to Xe^{10+}, an extrapolation of the parameters to ionization levels larger than Xe^{10+} does not seem possible. In any case, the maximal cross-sections decrease by a numerical factor of 40 from Xe^+ to Xe^{10+} and are expected to further decrease at higher ionic charges. Thus neglecting impact ionization of ions beyond Xe^{10+} constitutes a reasonable approximation.

3.2 Treatment of electron impact ionization energies of clusters

Electron impact ionization takes place if the kinetic energy of the impinging electron exceeds the ionization energy and if its impact parameter d is not larger than the effective radius $r = (\pi\sigma)^{1/2}$ of the particular ionization level, where σ is the corresponding cross-section. The implementation of electron impact ionizations in clusters requires the basic approximation that the cross-sections $\sigma_j(E)$ are unaffected by the ion-atom and ion-ion interactions within the cluster, and that the corresponding single atom cross-sections, equation (7), will be used. Some further modifications are required for the cluster impact ionization events as compared to those of isolated atoms [19]. First, atomic ionization energies are defined for an electron being moved to an infinite distance from the parent ion. But since the ions and electrons are initially located inside a cluster, the ejected electron must be placed at some finite distance from the parent ion, which requires corrections for the energetics. Second, an impact parameter refers to an infinite distance of the impinging electron before the impact. However, in the cluster the electron comes from a finite distance and is deflected by other particles of the cluster. Third, the velocity of the impinging electron prior

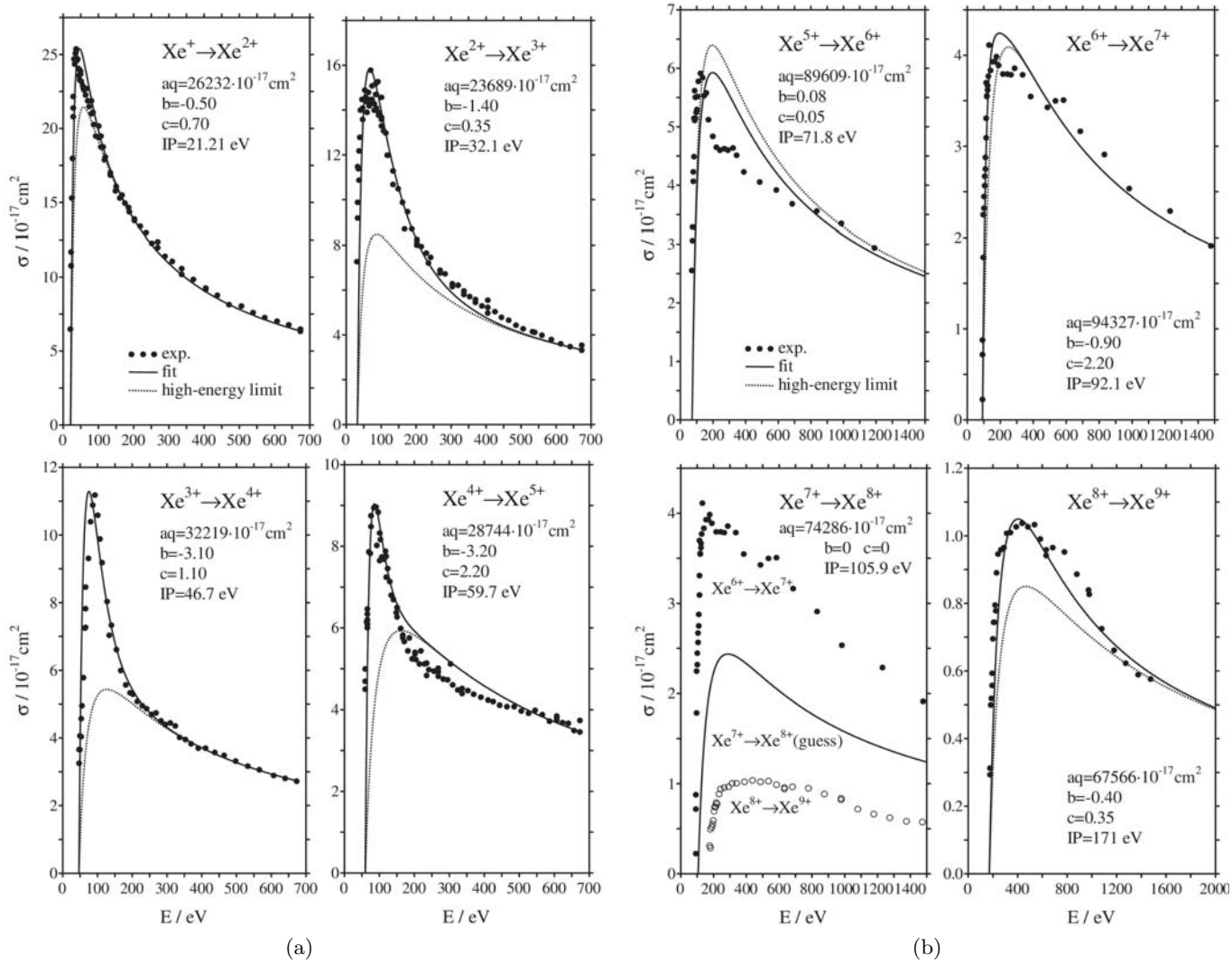

Fig. 1. The Lotz fits (solid lines), according to equation (7), of the energy dependence of the experimental cross-sections (dots) of the electron impact single ionizations of $Xe^{j+} + e \rightarrow Xe^{(j+1)+} + 2e$ for $1 \leq j \leq 10$. The values of the optimized parameters aq, b and c are given inside the panels. The high-energy limit function, equation (8), is given for comparison (dotted curve). The units of the parameter aq are $cm^2(eV)^2$ and the units of the ionization potential and the electron impact energy are eV. (a) The fits for $1 \leq j \leq 4$. The experimental data were taken from Achenbach et al. [33]. (b) The fits for $5 \leq j \leq 8$. The experimental cross-sections for $j = 5$ were taken from Griffin et al. [34], for $j = 6$ from Gregory et al. [35], and for $j = 8$ from Bannister et al. [36]. Since for $j = 7$ no experimental data are available, the parameter aq was chosen such that the $\sigma(E)$ function lies in the center of the gap between the experimental $j = 6$ and $j = 8$ data points. (c) The fits for $j = 9$ and $j = 10$. The experimental cross-sections were taken from Hofmann et al. [37].

and after the impact ionization as well as of the ejected electron are affected by the cluster environment.

In order to keep the computational effort small, the treatment of electron impact ionizations in our simulations rests on a simple sequential one-electron scheme. Only stepwise sequential ionizations, equation (4), are considered. The possibility of electron impact ionization is checked for all electrons at each electronic time step. An electron impact ionization is considered if a particular electron approaches an ion at a distance closer than 2 Å, which is considerably smaller than the interatomic distance of 4.3 Å at the beginning of the simulation. For a given electron-ion pair, ignoring all other ions and electrons of the cluster, the impact parameter is given by [40]

$$d = \frac{L}{\sqrt{2m_e E_{kin,\infty}}}, \tag{9}$$

where L is the absolute value of the angular momentum of the electron, m_e is the electron mass and $E_{kin,\infty}$ is the kinetic energy of the electron at infinity. Equation (9) rests on the fact that the electron velocity v_∞ at infinite distance is by definition perpendicular to the impact parameter d, so that in the vector product $\mathbf{L} = m\mathbf{r} \times \mathbf{v}$, of the position $\mathbf{r}$ and velocity $\mathbf{v}$ may be replaced by the corresponding scalar quantities d and v_∞, where $v_\infty = (2E_{kin,r}/m_e)^{1/2}$ can be obtained from the kinetic energy $E_{kin,\infty}$ of the electron at infinite distance to the ion. $E_{kin,\infty}$ can be calculated from the instantaneous kinetic energy $E_{kin,r}$ at the electron-ion distance r

$$E_{kin,\infty} = E_{kin,r} - \frac{q}{(r^6 + r_0^6)^{1/6}}. \tag{10}$$

The correction term in equation (10) accounts for the conversion of kinetic into potential energy (with a smoothing parameter r_0 [19,31]) when the electron is placed at an infinite distance from the ion. Equation (9) is valid for any potential. The potential enters only through the correction term of the kinetic energy, equation (10). Equations (9) and (10) are exact for the isolated ion-electron subsystem. The approximate nature of this treatment for clusters originates from the neglect of all other particles in the cluster. L, which is constant only for the isolated ion-electron pair, was evaluated when the electron-ion distance falls short of the 2 Å limit, i.e., at the instant when the possibility of an electron impact ionization has to be checked for.

The impinging and the ejected electron in the electron impact ionization are treated in a very simple way. At the impact ionization, the location of the impinging electron is kept unchanged. The ejected electron is placed at the same distance from the ion, but in an angular distance of 60° from the impinging electron. The kinetic energy T_{final}, available for both electrons after the impact ionization, is obtained by setting the total energies of the entire cluster before and after the impact ionization to be equal. In atomic units the equation for T_{final} is:

$$T_{final} = \frac{q_A + 1}{(r_{Ak}^6 + r_0^6)^{1/6}} - P + \sum_{a \neq A} \left(\frac{q_a}{(r_{ak}^6 + r_0^6)^{1/6}} \right) - \sum_{a \neq A} \left(\frac{q_a}{(r_{aA}^6 + r_0^6)^{1/6}} \right) - \sum_i \left(\frac{1}{(r_{ik}^2 + \bar{r}_0^2)^{1/2}} \right) + \sum_i \left(\frac{1}{(r_{iA}^2 + \bar{r}_0^2)^{1/2}} \right) + \frac{1}{2} v_l^2, \tag{11}$$

where A denotes the Xe^{q+} ion where the impact takes place, k is the ejected electron and l is the impact electron. q_A is the charge of ion A before the impact. The first term in equation (11) represents the potential energy of the ejected electron in the field of ion A after the impact ionization. P is the ionization energy for $Xe^{q+} \rightarrow Xe^{(q+1)+} + e$, and $-P$ is the binding energy of the electron k by the isolated ion A before the impact ionization. The third and the forth terms in equation (11) are the potential energy differences of the ejected electron k in the field of all other ions a, after and before the impact ionization, respectively. The fifth and the sixth terms are the potential energy differences of electron k in the field of all other electrons i including the impinging electron l. It is assumed that before the impact ionization electron k is located in the center of ion A, so that the distance of electron k to all other ions and electrons is r_{aA} and r_{iA}, respectively. $v_l^2/2$ is the kinetic energy of the impinging electron before the impact ionization. In our simulation the impinging and the ejected electrons were given the same velocity direction as the impinging electron before the impact. The absolute velocities were scaled so that the kinetic energy T_{final} is allocated to the two electrons by equal parts. Thus the velocities v'_k and v'_l after the impact ionizations are

$$v'_k = v'_l = \sqrt{\frac{T_{final}}{v_l^2}}. \tag{12}$$

While the total energy is conserved in this way, the linear and angular momenta are not, but this is a small error in view of the large cluster mass.

4 Time dependence of inner ionization

4.1 Time dependence of cluster ionization levels

Figure 2 presents the simulation results for the time dependence of the inner ionization levels of Xe_{2171} clusters, as induced by a Gaussian laser pulse, equations (1–3), with the temporal laser profile also being portrayed in Figure 2. The time dependent ionization levels for $I = 10^{15}$–10^{20} Wcm^{-2} are presented during a single laser pulse. The total number of electrons N_{ii} produced by inner ionization is given by

$$N_{ii} = N_{BSI} + N_{imp} \tag{13}$$

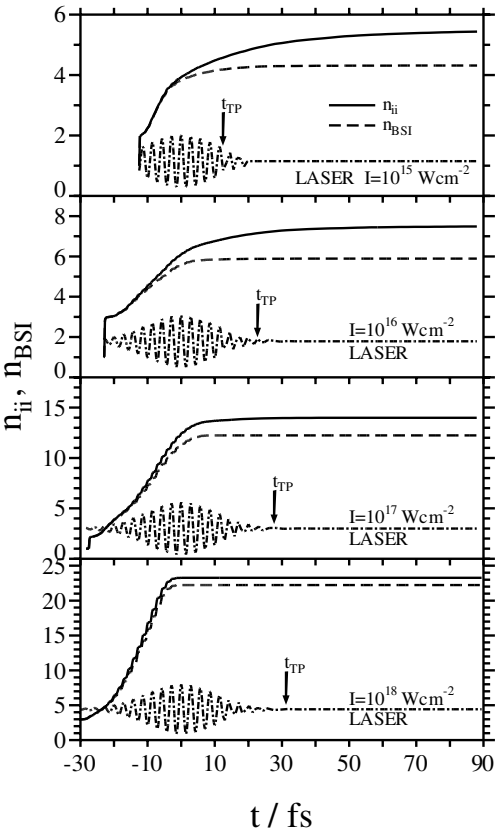

Fig. 2. The time dependence of the inner ionization levels, n_{ii}, and of the BSI levels, n_{BSI}, for Xe_{2171} clusters in the laser intensity domain $I = 10^{15}$–10^{18} Wcm^{-2}. The laser temporal profiles marked 'Laser' are also presented. The arrows mark the time $t_{TP} = -t_s$ for the characterization of the termination of the laser pulse.

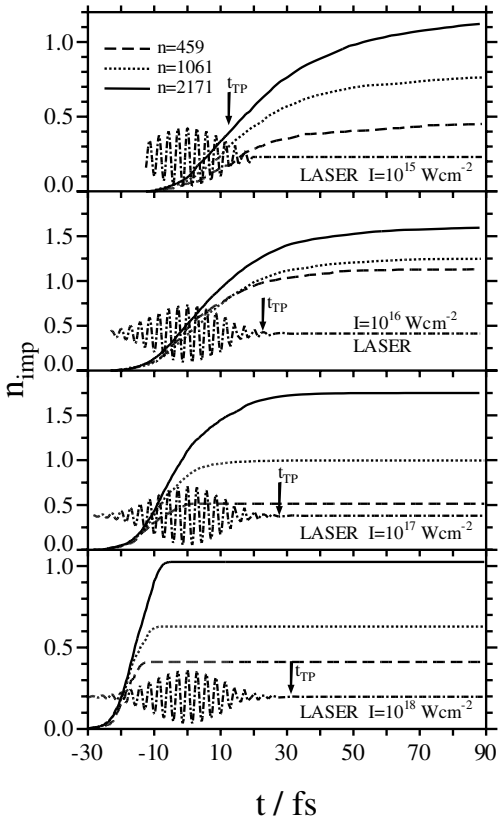

Fig. 3. The time dependence of the EII level n_{imp} for Xe_n (n = 459, 1061, 2171) clusters in the intensity domain $I = 10^{15}$–10^{18} Wcm^{-2}. The presentation of the laser pulse profile and the time t_{TP} are identical to those in Figure 2.

where N_{BSI} is the total number of electrons produced by BSI (mechanism (A)), while N_{imp} is the total number of electrons produced by EII (mechanism (B)). The ionization levels for a Xe_n cluster are given in terms of electrons depleted per constituent atom, with the total inner ionization level

$$n_{ii} = N_{ii}/n = n_{BSI} + n_{imp} \tag{14}$$

where the BSI level being $n_{BSI} = N_{BSI}/n$, and the EII level being $n_{imp} = N_{imp}/n$.

In Figure 2 we present typical data for the time dependence of the total ionization level n_{ii} for Xe_{2171} clusters coupled to laser fields ($I = 10^{15}$–10^{20} Wcm^{-2}), with the temporal profile of the laser pulses also being presented in the figure. Both BSI and EII contributions for cluster inner ionization are included in the n_{ii} data, equation (13), of Figure 2, while the $n_{BSI} = n_{ii} - n_{imp}$, equation (13), data, which are also presented in Figure 2, represent the contribution of the BSI mechanism. From these results we infer that the major contribution to the yield of the inner ionization process originates from the BSI mechanism.

The time dependence of $n_{ii}(t)$ at fixed I exhibits a monotonous increase with increasing t. At 'long-time', $t \simeq 90$ fs, $n_{ii}(t = 90\text{ fs}) \equiv n_{ii}^{(L)}$ reaches saturation for $I = 10^{18}$ Wcm^{-2} and near saturation for $I = 10^{15}$ Wcm^{-2} (Fig. 2). It will be instructive to compare the long-time values of $n_{ii}^{(L)}$, with the 'long time' values of the BSI yield $n_{BSI}(t = 90\text{ fs}) \equiv n_{BSI}^{(L)}$. From the 'long-time' data of Figure 2 we note that for $I = 10^{15}$–10^{16} Wcm^{-2} the $n_{ii}^{(L)}$ values are higher by about 15–25% than the $n_{BSI}^{(L)}$ data, while for higher intensities of $I = 10^{18}$ Wcm^{-2} the $n_{ii}^{(L)}$ and $n_{BSI}^{(L)}$ data nearly coincide. Over a large time interval, from the termination of the laser pulse up to $t = 90$ fs, $n_{BSI}(t)$ remains constant at the value of $n_{BSI}^{(L)}$, as the BSI mechanism is operative only when the laser is on. In contrast, for the lower intensities of $I = 10^{15}$ Wcm^{-2}, n_{ii} continues a modest increase after the termination of the laser pulse (Fig. 2), as the EII is still operative (Sect. 4.3). For a fixed cluster size, $n_{ii}^{(L)}$ increases with increasing I, i.e., for Xe_{2171}, $n_{ii}^{(L)}$ increases from $n_{ii}^{(L)} = 5.3$ at $I = 10^{15}$ Wcm^{-2} up to $n_{ii}^{(L)} = 23.5$ at $I = 10^{18}$ Wcm^{-2} (Fig. 2). This marked increase of $n_{ii}^{(L)}$ is mainly due to the enhancement of the BSI level at higher intensities.

Figure 3 portrays the time dependence, cluster size dependence and laser intensity dependence of the EII levels, $n_{imp}(t)$, equation (13), for Xe_n (n = 459–2171) clusters. At all cluster sizes and for all intensities $n_{imp}(t)$ reaches

saturation levels for $I = 10^{17}$–10^{18} Wcm^{-2} and a near-saturation level for $I = 10^{15}$–10^{16} Wcm^{-2} (Fig. 3). For a fixed cluster size, the long-time values $n_{imp}^{(L)}$ for EII (at $t = 90$ fs) exhibit a moderate, nonmonotonous I dependence falling in the range $n_{imp}^{(L)} = 0.4$–1.2 for $n = 459$ and $n_{imp}^{(L)} = 1.2$–1.6 for $n = 2171$ (Fig. 3). Concurrently, the relative EII levels, expressed in terms of $n_{imp}^{(L)}/n_{ii}^{(L)}$ for a fixed cluster size, markedly decrease with increasing the laser intensity (Figs. 2 and 3), e.g., for Xe_{2171}, $n_{imp}^{(L)}/n_{ii}^{(L)} = 0.21$ at $I = 10^{15}$–10^{16} Wcm^{-2}, $n_{imp}^{(L)}/n_{ii}^{(L)} = 0.13$ at $I = 10^{17}$ Wcm^{-2}, and $n_{imp}^{(L)}/n_{ii}^{(L)} = 0.04$ at $I = 10^{18}$ Wcm^{-2} (Figs. 2 and 3), while at $I = 10^{20}$ Wcm^{-2}, $n_{imp}^{(L)}/n_{ii}^{(L)} = 0.02$. This enhancement of $n_{imp}^{(L)}/n_{ii}^{(L)}$ with decreasing I is due to the marked decrease of $n_{ii}^{(L)}$, together with a modest change of $n_{imp}^{(L)}$ in this intensity domain (see Sect. 4.2).

The total ionization levels for BSI and EII (Figs. 2 and 3) increase with increasing t from $n_{BSI} = 1$ and $n_{imp} = 0$ at $t = t_s$ (Tab. 1). The laser pulse is switched off at the time t_{TP}, which is chosen as $t_{TP} = -t_s$ (Tab. 1). At $t = t_{TP}$, the BSI levels $n_{BSI}(t_{TP})$ reach saturation at all intensities (Fig. 2), as the BSI mechanism is operative only when the laser is switched on. The time dependence of $n_{imp}(t)$ (Fig. 3) manifests a qualitatively different pattern than $n_{BSI}(t)$ (Fig. 2). In the lower intensity domain of $I = 10^{15}$–10^{16} Wcm^{-2}, the initial increase of $n_{imp}(t)$ with increasing t is slower than of $n_{BSI}(t)$ (Figs. 2 and 3), manifesting the sequential nature of the nanoplasma production by BSI and its reactivity by EII. Furthermore, in this intensity domain the EII level at the termination of the laser pulse $n_{imp}(t_{TP})$ does not saturate after the termination of the laser pulse, in contrast to the contribution of the BSI mechanism referred to above. Rather, for $I = 10^{15}$–10^{16} Wcm^{-2}, $n_{imp}(t)$ continues to increase with increasing t at $t > t_{TP}$, manifesting the prevalence of the EII by a persistent nanoplasma (Sect. 4.2) after termination of the laser pulse. At the higher intensities of $I = 10^{17}$–10^{18} Wcm^{-2}, $n_{imp}(t)$ saturates at $t > t_{TP}$, reflecting on the depletion of the transient nanoplasma for this high intensity (Sect. 4.2), so that the EII process is switched off in this time domain.

The short-time behavior of the total inner ionization and EII levels (Figs. 4a and 4b) reflects on an abrupt increase of n_{ii} from $n_{ii} = 1$ to 3 for larger clusters ($n = 1061$, 2171) in the time domain where the laser exhibits one temporal cycle (Fig. 4). This abrupt increase of n_{ii} (Fig. 4a) manifests effective, sequential, nearly instantaneous (i.e., with two computational ionization intervals of 20 attoseconds, Sect. 2) two-electron ionization of Xe^+ with the formation of Xe^{3+}. The BSI $Xe \rightarrow Xe^2 \rightarrow Xe^{3+}$ occurs on the time scale which is shorter than one laser optical cycle (Fig. 4a). This abrupt increase in n_{ii} is not due to the EII mechanism, as the n_{imp} data (Fig. 4b) represent a gradual increase with increasing t in this time domain, where the laser exhibits 2–3 optical cycles. Accordingly, the dominating mechanism for nonsequential double ionization of

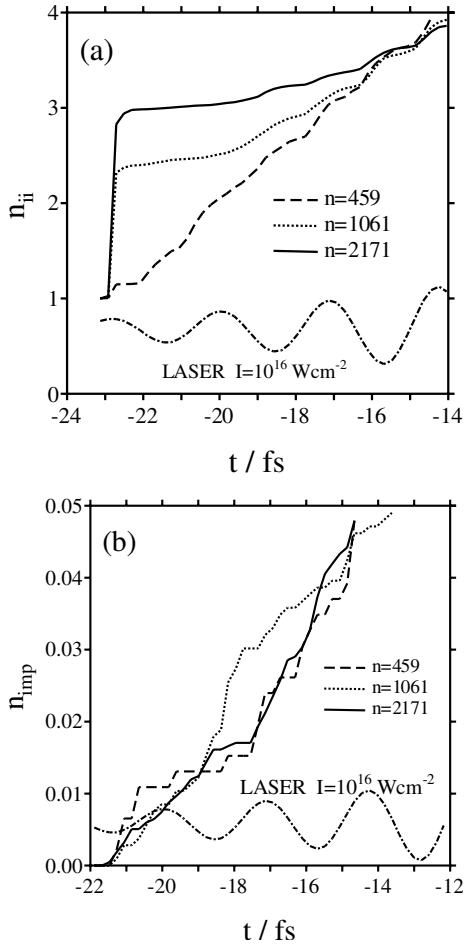

Fig. 4. The short-time behavior of the inner ionization level and the EII level of Xe_n ($n = 459$, 1061, 2171) clusters during the first laser cycles for the laser intensity of $I = 10^{16}$ Wcm^{-2}. The laser pulse profile (marked as 'Laser') is also presented in the figure. (a) The total inner ionization level. (b) The EII level.

Xe_n clusters at these high intensities of $I = 10^{18}$ Wcm^{-2} involves two BSI steps (see Sect. 5).

4.2 Cluster size dependence and ionization selectivity by electron impact ionization

In Figure 5 we present the cluster size dependence of the fraction of the long-time impact ionization level $n_{imp}^{(L)}/n_{ii}^{(L)}$ for Xe_n ($n = 55$–2171) clusters in the intensity domain of $I = 10^{15}$–10^{20} Wcm^{-2}. The $n_{imp}^{(L)}/n_{ii}^{(L)}$ data, which rest on reliable cross-sections for EII (Sect. 3), are plotted vs. R_0^2, following a previous presentation [31]. The present data are much more extensive and reliable than previously reported [31]. Over the entire intensity range the fraction of impact ionization increases monotonously with increasing R_0^2. The highest impact ionization fractions are obtained for the lower intensities of $I = 10^{15}$ and 10^{16} Wcm^{-2}, where $n_{imp}^{(L)}/n_{ii}^{(L)}$ assumes the value of 0.21 at $n = 2171$, 0.15–0.16 at $n = 1061$ and 0.09–0.14

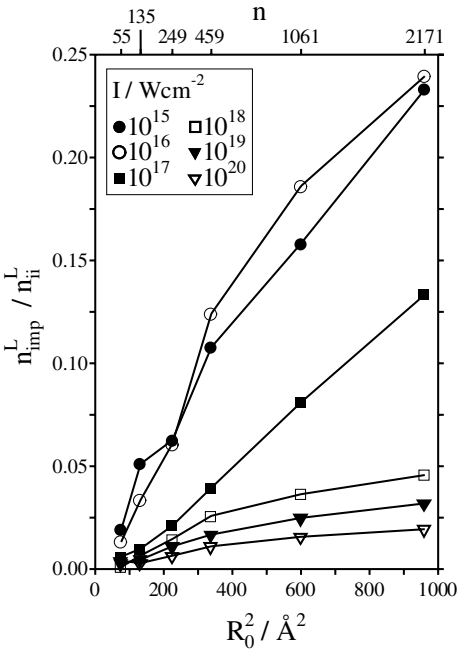

Fig. 5. The cluster size dependence of the fraction of the long-time impact ionization levels $n^{(L)}_{imp}/n^{(L)}_{ii}$ for Xe_n ($n = 55$–2171) clusters in the intensity range $I = 10^{15}$–10^{20} Wcm^{-2}. Data are presented for $n^{(L)}_{imp}/n^{(L)}_{ii}$ vs. R_0^2 for fixed values of I.

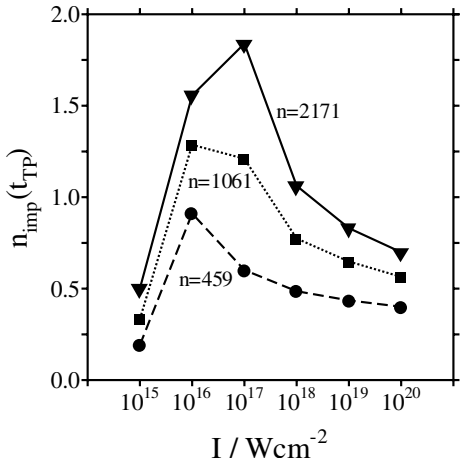

Fig. 6. The laser intensity dependence of the EII level $n_{imp}(t_{TP})$ at the termination of the laser pulse ($t_{TP} = -t_s$) for Xe_n ($n = 459$, 1061, 2171) clusters.

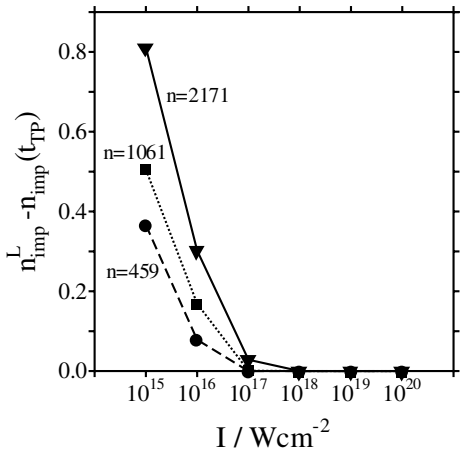

Fig. 7. The laser intensity dependence of the difference $\Delta n_{imp} = n^{(L)}_{imp} - n_{imp}\,(t_{TP})$ between the EII level at long time and at the termination of the laser pulse for Xe_n ($n = 459$, 1061, 2171) clusters.

at $n = 459$. The values of $n^{(L)}_{imp}/n^{(L)}_{ii}$ obtained from the present analysis of EII are higher by a numerical factor of ∼2 than those previously inferred [31] from crude estimates of the cross-sections for EII. At the lower intensities of $I = 10^{15}$–10^{16} Wcm^{-2} the R_0^2 size dependence of $n^{(L)}_{imp}/n^{(L)}_{ii}$ is nearly linear for $n < 1061$, and exhibits a slower increase at $n = 2171$ (Fig. 5). Increasing the intensity to $I = 10^{17}$ Wcm^{-2} (Fig. 5) $n^{(L)}_{imp}/n^{(L)}_{ii}$ increases nearly linearly with increasing R_0^2, in qualitative agreement with previous results [31], reaching the value of $n^{(L)}_{imp}/n^{(L)}_{ii} = 0.15$. For the highest intensity domain of $I = 10^{18}$–10^{20} Wcm^{-2}, the fractions of EII are very low with $n_{imp}/n_{ii} = 0.01$–0.05 (Fig. 5). The contribution of the EII mechanism is moderately small, although this mechanism should be incorporated for a quantitative study of inner ionization and electron dynamics in clusters. The laser intensity and cluster size domain appropriate for the study of EII in Xe_n clusters should involve large clusters ($n \gtrsim 2000$) and lower intensities ($I = 10^{15}$–10^{16} Wcm^{-2}).

The cluster size and laser intensity dependence of the impact ionization level reveals the following features:

(1) an increase of $n_{imp}(t_{TP})$ with increasing n at a fixed value of I (Fig. 3);
(2) at a fixed cluster size, $n_{imp}(t_{TP})$ increases with increasing I in the range $I = 10^{15}$–10^{17} Wcm^{-2}, reaches a maximum at $I = 10^{17}$ Wcm^{-2} and then decreases in the range $I = 10^{17}$–10^{18} Wcm^{-2} (Fig. 6);
(3) the overall nonuniform change of $n_{imp}(t_{TP})$ for fixed values of n (Fig. 6) is about ∼2 over the intensity range of $I = 10^{15}$–10^{18} Wcm^{-2}. This nonuniform increase of $n_{imp}(t_{TP})$ with increasing I (Fig. 6) is lower than the uniform increase of n_{BSI} at a fixed value of n by a numerical factor of ∼5 over this intensity domain of $I = 10^{15}$–10^{18} Wcm^{-2} (Fig. 2);
(4) the cluster size dependence of the 'long time' EII levels $n^{(L)}_{imp}$ (Sect. 4.1) exhibit similar trends to those of $n_{imp}(t_{TP})$. At a fixed value of I, $n^{(L)}_{imp}$ increases with increasing the cluster size (Fig. 3). On the other hand, at a fixed value of n, $n^{(L)}_{imp}$ exhibits a nonuniform dependence on I, increasing in the range $I = 10^{15}$–10^{17} Wcm^{-2}, manifesting a maximum at $I = 10^{17}$ Wcm^{-2} and decreasing in the range of $I = 10^{17}$–10^{18} Wcm^{-2};
(5) The difference $\Delta n_{imp} = n^{(L)}_{ii} - n_{ii}(t_{TP})$ in the EII level at a 'long time' and at $t = t_{TP}$ (Fig. 7), reflects on the ionization dynamics by the nanoplasma in the time domain when the laser pulse is switched off.

Highlight Paper

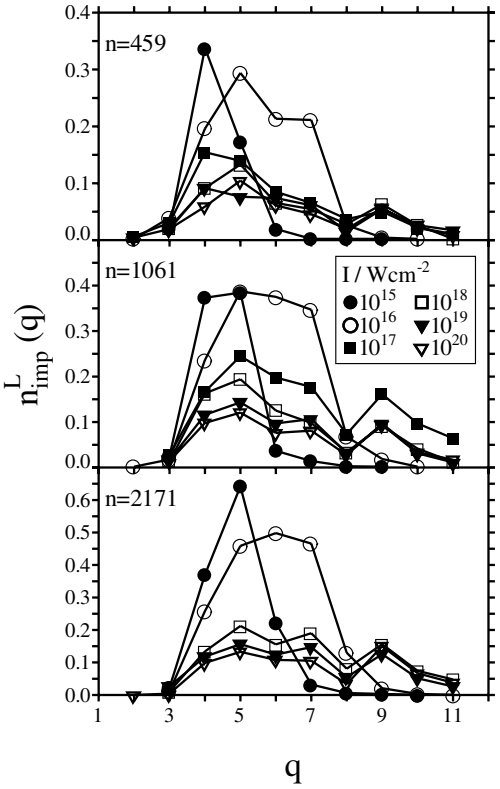

Fig. 8. The distribution $n_{imp}(q)$ of the charges of the Xe^{q+} ions produced by EII of Xe_n ($n = 459$, 1061, 2171) clusters in the intensity range $I = 10^{15}$–10^{20} Wcm^{-2}.

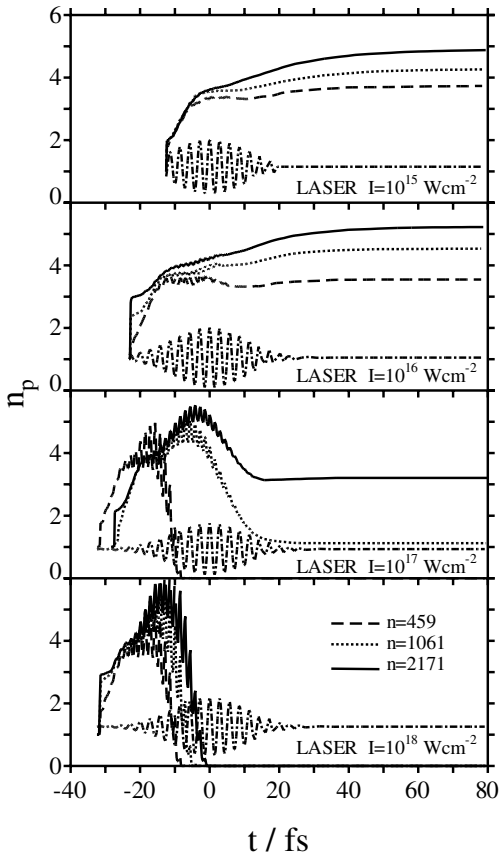

Fig. 9. The time dependence of the nanoplasma population n_p per atom (see text) in Xe_n ($n = 459$, 1061, 2171) clusters induced by the laser fields (with the laser profile, marked 'Laser', shown in each panel) in the intensity range $I = 10^{15}$–10^{18} Wcm^{-2}. Note the qualitative difference between the persistent nanoplasma at $I = 10^{15}$–10^{16} Wcm^{-2} and the transient nanoplasma at $I = 10^{18}$ Wcm^{-2}.

In the high intensity range of $I = 10^{17}$–10^{18} Wcm^{-2}, Δn_{imp} is negligibly small (Fig. 7), due to the depletion effects of the transient nanoplasma [28] (Sect. 5). On the other hand, for the lower intensity range Δn_{imp} is quite large, e.g., for Xe_{2171}, varying from $\Delta n_{imp} = 0.9$ at $I = 10^{15}$ Wcm^{-2} to $\Delta n_{imp} = 0.4$ at $I = 10^{16}$ Wcm^{-2} (Fig. 7). In this intensity domain EII prevails by the energetic nanoplasma under 'laser free' conditions (Sect. 5).

Of interest is the ionization level distribution of the charges of the Xe^{q+} ions produced by EII (Fig. 8). From our simulations, where both BSI and EII mechanisms prevail, the (small) contribution of Xe^{q+} ions produced by EII reveals a cluster size independent, but intensity dependent, ionization level distribution (Fig. 8). For the lowest intensity of $I = 10^{15}$ Wcm^{-2} the distribution of Xe^{q+} ions produced by EII peaks at $q_{max} = 3$, while at $I = 10^{16}$ Wcm^{-2} the peak of this distribution shifts to $q = 4$–5 (Fig. 8). For the highest intensities of $I = 10^{18}$–10^{20} Wcm^{-2} the distribution of the (very small) number of Xe^{q+} ions produced by EII is bimodal with a broad peak at $q_{max} \simeq 6$ and a sharper peak at $q_{max} \simeq 9$ (Fig. 8). The EII occurs in parallel to and sequentially with the BSI. The dominating BSI mechanism results in a higher charge of the Xe^{q+} ions with increasing the intensity. Accordingly, the sequential EII minority channel will manifest higher values of q_{max} at higher intensities. The relative yields of EII are sufficiently small so that this mechanism does not affect the total distribution of Xe^{q+} ions produced by inner ionization, for which the BSI mechanism dominates.

5 Discussion

The EII mechanism provides an avenue for inner ionization of large clusters triggered by an energetic nanoplasma in a system of a cluster coupled to an ultraintense laser field (at $t \leq t_{TP}$), and in a laser-free system (at $t \geq t_{TP}$). From the foregoing simulation data we inferred on the cluster size and laser intensity dependence of the EII levels. The following effects contribute to the EII dynamics and yields: (1) kinetic effects on EII. Increasing the cluster size at fixed I will result in the increase of the total number of the nanoplasma electrons $N_p = n_p n$, where the nanoplasma population is $n_p = (n_{ii} - n_{oi})$, with n_{oi} being the cluster outer ionization level [31]. In Figure 9 we present the time dependence of the nanoplasma population $n_p(t)$. The cluster size dependence at fixed I (Fig. 9) exhibits an increase of n_p with increasing the cluster size.

In the size domain $n = 459{-}2171 n_p$ increases by ∼20% for $I = 10^{15}{-}10^{16}$ Wcm^{-2}, while the maximal value of n_p at $I = 10^{18}$ Wcm^{-2} increased by 25% in this size domain (Fig. 9). Accordingly, at fixed I, the value of N_P (at $t = t_{TP}$ or at its maximum) manifests an increase by about 20–25% in the size domain of $n = 459{-}2171$. The time dependence of $n_p(t)$ provides an important ingredient for the understanding of the dependence of $n_{imp}(t_{PT})$ on the laser intensity at a fixed cluster size. In the lower intensity domain of $I = 10^{15}{-}10^{16}$ Wcm^{-2}, $n_p(t)$ vs. t for Xe_{2171} (Fig. 9) gradually increases, reaching at $t = t_{PT}$ values of $n_p(t_{PT}) \simeq 4$ at $I = 10^{15}$ Wcm^{-2}, $n_p(t_{PT}) = 4.5$ at $I = 10^{16}$ Wcm^{-2}, while for the higher intensities the maximal value of n_p for Xe_{2171} is 5.5 at $I = 10^{17}$ Wcm^{-2} and 6.0 at $I = 10^{18}$ Wcm^{-2}. Thus N_P increases with increasing I at a fixed cluster size. In order to provide a comprehensive picture for the intensity dependence of $n_{imp}(t)$ (Fig. 6) one has to account for energetic and dynamic effects of the nanoplasma, which will not be considered.

(2) Nanoplasma energetics. In the lower intensity domain ($I = 10^{15}{-}10^{16}$ Wcm^{-2}), the energy of the nanoplasma is lower than for the higher intensities ($I = 10^{18}{-}10^{20}$ Wcm^{-2}) [28]. Simulations of the nanoplasma energetics in Xe_n ($n = 1061$) clusters [28] revealed that the energy distribution $\Delta\varepsilon$ of the electrons in the nanoplasma is $\Delta\varepsilon \simeq 50{-}400$ eV and the average nanoplasma energy is $\varepsilon_{av} \simeq 50$ eV for $I = 10^{16}$ Wcm^{-2}. For $I = 10^{18}$ Wcm^{-2} the energy distribution range of the nanoplasma is 0.5–3 keV and $\varepsilon_{av} \simeq 1$ keV [28]. A cursory examination of the Xe electron impact ionization cross-sections (Fig. 1) in the range of Xe^{q+}, which correspond to the maximal values of N_{imp} (Fig. 8), reveals that the maximal charge q_{max} increases with increasing I, due to the enhancement of the population of higher charged ions by the BSI mechanism. Thus for $I = 10^{16}$ Wcm^{-2}, where $q_{max} \simeq 3$, $\sigma(E)$ peaks around $\Delta\varepsilon = 80{-}100$ eV (Fig. 1), which falls in the energy range of $\Delta\varepsilon$ for this intensity. For $I = 10^{18}$ Wcm^{-2}, where $q_{max} = 6$ and 9, the maximal value of the cross-section (Fig. 8) is at $\Delta\varepsilon = 200{-}400$ eV, which is lower ε_{av}. EII cross-sections at $q_{max} = 3$ are higher by about one-order of magnitude than those at $q_{max} = 6{-}9$ (Fig. 1). Accordingly, we expect that the EII cross-sections are enhanced at lower laser intensities due to he increase of the nanoplasma energy and the increase of the EII cross-sections in the lower laser intensity domain.

(3) Dynamics of nanoplasma. Our simulations reveal a quantitative difference between the dynamics of the nanoplasma in different intensity domains (Fig. 9). In the higher intensity domain of $I = 10^{18}$ Wcm^{-2} (Fig. 9), the nanoplasma is transient, with a complete depletion at $t - t_s = 30$ fs for $n = 459$, $t - t_s = 35$ fs for $n = 1061$ and $t - t_s = 40$ fs for $n = 2171$, so that the temporal depletion threshold increases with increasing the cluster size. EII can prevail only on the ultrashort time scales of $t \leq 40$ fs in this intensity domain. On the other hand, in the lower intensity domain of $I = 10^{15}$ Wcm^{-2} (Fig. 9), the nanoplasma is persistent over the time scale of $t - t_s > 100$ fs and no indication of nanoplasma depletion is manifested. Accordingly, the longer lifetime of the nanoplasma for $I = 10^{15}{-}10^{16}$ Wcm^{-2} renders the EII yield to be more efficient in the lower intensity domain.

From this analysis of the effects of nanoplasma kinetics, energetics and dynamics the following conclusions emerge regarding the EII yields:

(i) cluster size dependence of EII yields. The enhancement of $n_{imp}(t_{TP})$ with increasing the cluster size at a fixed laser intensity (Figs. 2, 3 and 6) is due to the kinetic effect of the increase of the total number of the nanoplasma electrons with increasing n at a fixed value of I (Figs. 2, 3 and 9);

(ii) intensity dependence of the EII yields during the laser pulse. The increase of $n_{imp}(t_{TP})$ with increasing I at a fixed cluster size in the intensity range $I = 10^{15}{-}10^{17}$ Wcm^{-2} (Fig. 6) is attributed to a delicate balance between the kinetic effect of the increase of the total number of the nanoplasma electrons, which increase the EII yield, and the increase of ε_{av} with increasing I, which contributes to the decrease of the EII yield. [The maximum in $n_{imp}(t_{TP})$ at $I = 10^{17}$ Wcm^{-2}, together with the decrease of $n_{imp}(t_{TP})$ at $I = 10^{17}{-}10^{18}$ Wcm^{-2} (Fig. 6), reflects on the dynamic effects of nanoplasma depletion at the highest intensities (Fig. 9), which lead to the decrease of the EII yield.];

(iii) 'laser-free' EII. When the nanoplasma is persistent at $I = 10^{15}{-}10^{16}$ Wcm^{-2} (Fig. 6) EII can be induced by the nanoplasma after the termination of the laser pulse, i.e., at $t > t_{TP}$. The finite values of Δn_{ii} at the lower laser intensities (Fig. 8) are due to the EII by the energetic persistent nanoplasma in the 'laser free' system. Of course, the energetic nanoplasma is produced by coupling of the cluster to the laser field, with concurrent EII induced after the laser pulse is switched off.

The present study of EII in a coupled cluster-ultraintense laser system provides novel information on reactive femtosecond and attosecond electron dynamics induced by a nanoplasma in a large finite system. Laser radiation chemistry effects of the nanoplasma are of interest in the context of control of electron dynamics and ionization levels of clusters [7,9,20,28]. The present studies have to be extended for experimental, theoretical and computational exploration of control of electron-nuclear cluster dynamics induced by ultraintense laser fields.

Ultrafast electron dynamics on the time scale of a few laser optical cycles constitutes a new and exciting development [41–43]. The short-time ionization of Xe_n clusters on the time scale of a single optical cycle (Fig. 4a) corresponds to cluster nonsequential double ionization (NDI), which was previously studied for atoms [43–45]. There is a qualitative difference between the $Xe^+ \rightarrow Xe^{3+}$ NDI in Xe_n clusters at $I = 10^{18}$ Wcm^{-2} studied herein, and the NDI of inert gas atoms, e.g., Ar, which proceeds via $Ar \rightarrow Ar^+ + e \rightarrow Ar^{2+} + 2e$ at $I = 3.5 \times 10^{14}$ Wcm^{-2} [43]. The latter case involves an $(e, 2e)$ process, with an electron produced by BSI inducing a second ionization by EII. In the

Highlight Paper

present case of two-electron ionization of Xe_n clusters at very large fields (Fig. 4a), the dominating mechanisms for both nonsequential ionization steps involves BSI. It will be interesting to conduct simulations of short-time ionization dynamics on the time scale of a few laser cycles in Xe_n and Ar_n clusters with modified initial conditions. While in the present study, which focuses on extreme cluster multielectron ionization we have chosen a $(Xe^+)_n$ cluster at $t = t_s$, the exploration of NDI in clusters will initially involve a neutral Xe_n cluster.

This research was supported by the Deutsche Forschungsgemeinschaft (SFB 450) on "Analysis and Control of Ultrafast Photoinduced Reactions".

References

1. J. Zweiback, R.A. Smith, T.W. Cowan, G. Hays, K.B. Wharton, V.P. Yanovsy, T. Ditmire, Phys. Rev. Lett. **84**, 2634 (2000)
2. R.W. Madison, P.K. Patel, D. Price, A. Edens, M. Allen, T.E. Cowan, J. Zweiback, T. Ditmire, Phys. Plasmas **11**, 270 (2004)
3. V. Kumarappan, M. Krishnamurthy, D. Mathur, Phys. Rev. A **67**, 063207 (2003)
4. G. Grillon, Ph. Balcou, J.-P. Chambaret, D. Hulin, J. Martino, S. Moustaizis, L. Notebaert, M. Pittman, Th. Pussieux, A. Rousse, J.-Ph. Rousseau, S. Sebban, O. Sublemontier, M. Schmidt, Phys. Rev. Lett. **89**, 065005 (2002)
5. T. Ditmire, J.W.G. Tisch, E. Springate, M.B. Mason, N. Hay, J.P. Marangos, M.H.R. Hutchinson, Phys. Rev. Lett. **78**, 2832 (1997)
6. K. Kondo, A.B. Borisov, C. Jordan, A. McPherson, W.A. Schroeder, K. Boyer, C.K. Rhodes, Phys. Rev. B **30**, 2707 (1997)
7. T. Ditmire, E. Springate, J.W.G. Tisch, Y.L. Shao, M.B. Mason, N. Hay, J.P. Marangos, M.H.R. Hutchinson, Phys. Rev. A **57**, 369 (1998)
8. M. Lezius, S. Dobosz, D. Normand, M. Schmidt, Phys. Rev. Lett. **80**, 261 (1998)
9. E. Springate, N. Hay, J.W.G. Tisch, M.B. Mason, T. Ditmire, M.H.R. Hutchinson, J.P. Marangos, Phys. Rev. A **57**, 063201 (2000)
10. K.J. Mendham, N. Hay, M.B. Mason, J.W.G. Tisch, J.P. Marangos, Phys. Rev. A **64**, 055201 (2001)
11. M. Schnürer, S. Ter-Avetisyan, H. Stiel, U. Vogt, W. Radloff, M. Kalashnikov, W. Sandner, P.V. Nickles, Eur. Phys. J. D **14**, 331 (2001)
12. M. Lezius, V. Blanchet, M.Yu. Ivanov, A. Stolow, J. Chem. Phys. **117**, 1575 (2002)
13. Y. Fukuda, K. Yamakawa, Y. Akahane, M. Aoyama, N. Inoue, H. Ueda, Y. Kishimoto, Phys. Rev. A **67**, 061201 (2003)
14. J. Schulz, H. Habnitz, T. Laarmann, S. Gürtler, W. Laasch, A. Swideriski, Th. Möller, A.A.B. de Castro, Nucl. Instr. Meth. Phys. A **507**, 572 (2003)
15. S. Zamith, T. Martchenko, Y. Ni, S.A. Aseyev, H.G. Muller, M.J.J. Vrakking, Phys. Rev. A **70**, 011201 (2004)
16. J. Purnell, E.M. Snyder, S. Wei, A.W. Castleman Jr., Chem. Phys. Lett. **229**, 333 (1994)
17. J.W.G. Tisch, N. Hay, E. Springate, E.T. Gumbrell, M.H.R. Hutchinson, J.P. Marangos, Phys. Rev. A **60**, 3076 (1999)
18. T. Ditmire, Phys. Rev. A **57**, R4094 (1998)
19. I. Last, J. Jortner, Phys. Rev. A **62**, 013201 (2000)
20. K. Ishikava, T. Blendski, Phys. Rev. A **62**, 063204 (2000)
21. I. Last, J. Jortner, Phys. Rev. A **64**, 063201 (2001)
22. V.P. Krainov, A.S. Roschchupkin, Phys. Rev. A **64**, 063204 (2001)
23. Ch. Siedschlag, J.M. Rost, Phys. Rev. A **67**, 013404 (2003)
24. I. Last, J. Jortner, J. Chem. Phys. **121**, 3030 (2004)
25. I. Last, J. Jortner, J. Chem. Phys. **121**, 8329 (2004)
26. R. Stoian, D. Ashkenasi, A. Rosenfeld, E.E.B. Campbell, Phys. Rev. B **62**, 13167 (2000)
27. U. Andiel, K. Eidmann, K. Witte, I. Uschmann, E. Förster, Appl. Phys. Lett. **80**, 198 (2002)
28. I. Last, J. Jortner, J. Chem. Phys. **120**, 1348 (2004)
29. C. Rose-Petruck, K.J. Schafer, K.R. Wilson, C.P.J. Barty, Phys. Rev. A **55**, 1182 (1997)
30. W. Lotz, Z. Phys. **216**, 241 (1968)
31. I. Last, J. Jortner, J. Chem. Phys. **120**, 1336 (2004)
32. D.P. Almeida, J. Electron Spectrosc. Relat. Phenom. **122**, 1 (2002)
33. C. Achenbach, A. Mueller, E. Salzborn, R. Becker, J. Phys. B **17**, 1405 (1984)
34. D.C. Griffin, C. Bottcher, M.S. Pindzola, S.M. Younger, D.C. Gregory, D.H. Crandall, Phys. Rev. A **29**, 1729 (1984)
35. D.C. Gregory, D.H. Crandall, Phys. Rev. A **27**, 2338 (1983)
36. M.E. Bannister, D.W. Mueller, L.J. Wang, M.S. Pindzola, D.C. Griffin, D.C. Gregory, Phys. Rev. A **38**, 38 (1988)
37. G. Hofmann, J. Neumann, U. Pracht, K. Tinschert, M. Stenke, R. Voelpel, E. Salzborn, *AIP Conference Proceedings* **274** (International Conference on the Physics of Highly Charged Ions, 1992), 485 (1993)
38. W. Lotz, Z. Phys. **206**, 205 (1967)
39. R.D. Cowan, *The Theory of Atomic Structure and Spectra* (University of California Press, Berkeley, 1981)
40. L.D. Landau, E.M. Lifshitz, *Mechanics* (Pergamon Press, Oxford, 1960)
41. M. Nisoli, S. De Silvestri, O. Svelto, R. Szipcs, K. Ferencz, Ch. Spielmann, S. Sartania, F. Krausz, Opt. Lett. **22**, 522 (1997)
42. G. Steinmeyer, D.H. Sutter, L. Gallmann, N. Matuschek, U. Keller, Science **286**, 1507 (1999)
43. X. Liu, H. Rottke, E. Eremina, W. Sandner, E. Goulielmakis, K.O. Keeffe, M. Lezius, F. Krausz, F. Lindner, M.G. Schätzel, G.G. Paulus, H. Walther, Phys. Rev. Lett. **93**, 263001 (2004)
44. P.B. Corkum, Phys. Rev. Lett. **71**, 1994 (1993)
45. C. Figueira de Morisson Faria, X. Liu, W. Becker, H. Schomerus, Phys. Rev. A **69**, 021402 (R) (2004)